sample amounts (~ a few femtomoles) without any organic matrices. In contrast to traditional MALDI-MS, this novel substrate showed no sweet-spot problem, that is, equal sensitivity on the whole substrate surface, and the spectra also have fewer obstacle peaks. Pt nanoflowers also showed good performance (both high sensitivity and high molecular weight) for SALDI-MS of various biomolecules, including peptides and phospholipids. Pt nanoflower-coupled MS techniques would develop metabolomics research and mass imaging to achieve global interpretation of cell behavior and organ function and also industrial material studies such as synthetic polymers and additives.

Acknowledgment. This work was partially supported by a Grant-in-Aid for Scientific Research (B) and by the Research and Development Organization of Industry−University Cooperation funding from the Ministry of Education, Culture, Sports, Science, and Technology of Japan, and by Grants-in-Aid for Scientific Research (Nos. 17655059, 18710102, 18310069, and 19350045) from the Japan Society for the Promotion of Science. T.Y. is also thankful for the partial financial support from Health and Labour Science Research Grants for Research on Risk Assessment of Chemical Substances (H18-Chem-General-006) from the Ministry of Health, Labour and Welfare.

Supporting Information Available: HRSEM image of secondary aggregates of platinum nanoparticles and mass spectrum of angiotensin. This material is available free of charge via the Internet at http://pubs.acs.org.

References and Notes

(1) El-Sayed, M. A. *Acc. Chem. Res.* **2001**, *34*, 257.
(2) Daiel, M.-C.; Astruc, D. *Chem. Rev.* **2004**, *104*, 293.
(3) Schiltz, D. A. *Curr. Opin. Biotechnol.* **2003**, *14*, 13.
(4) Elghanian, R.; Storhoff, J. J.; Mucic, R. C.; Letsinger, R. L.; Mirkin, C. A. *Science* **1997**, *277*, 1078.
(5) Nie, S.; Emory, S. R. *Science* **1997**, *275*, 1102.
(6) Tanaka, K.; Waki, H.; Ido, Y.; Akita, S.; Yoshida, Y.; Yoshida, T. *Rapid Commun. Mass Spectrom.* **1988**, *2*, 151.
(7) Karas, M.; Hillenkamp, F. *Anal. Chem.* **1988**, *60*, 2299.
(8) Dreisewerd, K. *Chem. Rev.* **2003**, *103*, 395.
(9) Montaudo, G.; Samperi, F.; Montaudo, M. S. *Prog. Polym. Sci.* **2006**, *31*, 277.
(10) Schiller, J.; Suss, R.; Arnhold, J.; Fuchs, B.; Lessig, J.; Muller, M.; Petkovic, M.; Spalteholz, H.; Zschoring, O.; Arnold, K. *Prog. Lipid. Res.* **2004**, *43*, 449.
(11) Zumbuhl, S.; Knochenmuss, R.; Wulfert, S.; Dubois, F.; Dale, M. J.; Zenobi, R. A. *Anal. Chem.* **1998**, *70*, 707.
(12) Ugarov, M. V.; Egan, T.; Khabashesku, D. V.; Schultz, J. A.; Peng, H. Khabashesku, V. N.; Furutani, H.; Prather, K. S.; Wang, H.-W. J.; Jackson, S. N.; Woods, A. S. *Anal. Chem.* **2004**, *76*, 6734.
(13) Wei, J.; Buriak, J. M.; Siuzdak, G. *Nature* **1999**, *399*, 243.
(14) Trauger, S. A.; Go, E. P.; Shen, Z.; Apon, J. V.; Compton, B. J.; Bouvier, E. S. P.; Finn, M. G.; Siuzdak, G. *Anal. Chem.* **2004**, *76*, 4484.
(15) Okuno, S.; Arakawa, R.; Okamoto, K.; Matsui, Y.; Seki, S.; Kozawa, T.; Tagawa, S.; Wada, Y. *Anal. Chem.* **2005**, *77*, 5364.
(16) Chen, C.-T.; Chen, Y.-C. *Anal. Chem.* **2004**, *76*, 1453.
(17) Teng, C.-H.; Ho, K.-C.; Lin,; Chen, Y.-C. *Anal. Chem.* **2004**, *76*, 4337.
(18) Peterson, D. S. *Mass Spectrom. Rev.* 2007, **26**, 19.
(19) McLean, J. A.; Stumpo, K. A.; Russell, D. H. *J. Am. Chem. Soc.* **2005**, *127*, 5304.
(20) Lee, H.; Habas, S. E.; Kweskin, S.; Butcher, D.; Somorjai, G. A.; Yang, P. *Angew. Chem., Int. Ed.* **2006**, *45*, 7824.
(21) Tu, W.; Takai, K.; Fukui, K.-I.; Miyazaki, A.; Enoki, T. *J. Phys. Chem. B* **2003**, *107*, 10134.
(22) Su, C.-L.; Tseng, W.-L. *Anal. Chem.* **2007**, *79*, 1626.
(23) *Caution!* Addition of $NaBH_4$ at once causes an abundance of hydrogen bubbles. A very large flask should be used in a draft chamber for safety. $NaBH_4$ may ignite, especially under high humidity.
(24) Chen, C.-T.; Chen, Y.-C. *Rapid Commun. Mass Spectrom.* **2004**, *18*, 1956.
(25) Chen, C.-T.; Chen, Y.-C. *Anal. Chem.* **2005**, *77*, 5912.
(26) Go, E. P.; Apon, V. J.; Luo, G.; Saghatelian, A.; Daniels, R. H.; Sahi, V.; Dubrow, R.; Cravatt, B. F.; Vertes, A.; SiuzdaK, G. *Anal. Chem.* **2005**, *77*, 1641.
(27) Alimpiev, S.; Nikiforov, S.; Karavanskii, V. *J. Chem. Phys.* **2001**, *115*, 1891.
(28) Buffat, P.; Borel, J. P. *Phys. Rev. A* **1976**, *13*, 2287.

Fabrication of Submillimeter-sized Gold Plates from Thermal Decomposition of $HAuCl_4$ in Two-component Ionic Liquids

Hideya Kawasaki,[1] Tetsu Yonezawa,[2] Kouhei Nishimura,[1] and Ryuichi Arakawa*[1]
[1]*Department of Applied Chemistry, Faculty of Engineering, Kansai University, 3-3-35 Yamate-cho, Suita, Osaka 564-8680*
[2]*Department of Chemistry, Graduate School of Science, The University of Tokyo, 7-3-1 Hongo, Bunkyo-ku, Tokyo 113-0033*

(Received May 21, 2007; CL-070547; E-mail: arak@ipcku.kansai-u.ac.jp)

We first report the fabrication of submillimeter-sized Au plates (up to about 1 mm in size) through the simple thermal decomposition of $HAuCl_4$ in two-component ionic liquids of 1-butyl-3-methylimidazolium hexafluorophosphate (C4ImPF6) and 1-octyl-3-methylimidazolium hexafluorophosphate (C8ImPF6), which were about ten times larger sizes than those from the single-component ionic liquid of the either.

Over the past few decades, a considerable number of studies have been conducted on metal-nanostructured materials owing to their unique physical and chemical properties that strongly depend on their size and shape.[1] Thus, the concern with the size- or shape-controlled fabrication of metal nanoparticles,[2,3] such as rods,[4] wires,[5] plates,[6] and branched multipods,[7] has been growing. Gold (Au) plates are of particular interest because of their potential applications of electrochemistry and producing new nanodevices.[8,9] Some groups have reported the fabrications of two-dimensional gold nanostructures, called Au nano- or microplates in the size range from 50 nm to 100 μm.[9] However, there have been few studies that tried to fabricate millimeter-scale Au plates with nanolevel thickness, even though such extremely large crystals could be useful in microelectronic systems and the understanding the mechanism of shape-controlled growth from the nanometer to the millimeter scale. Recently, Li et al. reported high-yield production of Au plates with several ten micrometer-scale size and the thickness of 50 nm in microwave heating of $HAuCl_4$ in an ionic liquid, 1-butyl-3-methylimidazolium tetrafluoroborate.[10] It was suggested that the two-dimensional polymeric layer in the ionic liquid could act as the template structure for the formation of Au nanoplates.

Here, we report for the first time the formation of submillimeter-sized Au plates through the simple thermal decomposition of $HAuCl_4$ in two-component ionic liquids of 1-butyl-3-methylimidazolium hexafluorophosphates (C4ImPF6) and 1-octyl-3-methylimidazolium hexafluorophosphates (C8ImPF6). It is considered that the preferential adsorption of amphiphilic molecules from solutions onto different crystal faces influences the growth of nanometals into various shapes and sizes by controlling the growth rates. The adsorption of ionic liquids onto Au surfaces, which depends on the composition of ionic liquid mixture, should contribute to the formation of Au plates.

In a typical fabrication of submillimeter-sized Au plates, $HAuCl_4 \cdot 3H_2O$ (100 mg/mL) was dissolved in 1:1 mixture of C4ImPF6 and C8ImPF6 (5 mL). The extremely large size Au plates were obtained by a slow reduction of gold precursor with a gradual growth of Au plates in mixed ionic liquids by electrically heated plate at 220 °C for 2 h to give a golden precipitate, which was collected, washed with ethanol, and dried under air stream. Similar process was employed for the preparation of Au plates in a single component ionic liquid, except that the different heating temperatures were used for the C4ImPF6 (270 °C) and the C8ImPF6 (210 °C).

We have found high-yield production of submillimeter-sized Au plates (up to about 1 mm in size, see Graphical Abstract) through the thermal decomposition of $HAuCl_4$ in the two-component ionic liquids of C4ImPF6 and C8ImPF6. Figure 1 shows the typical microscope image of submillimeter-sized Au plates. The sizes of Au plates mainly range from 50 to 900 μm in the micrometer-scale (see the histogram of Figure 1), which were about ten times larger sizes than those from the single-component ionic liquid (up to ca. 80 μm in size for C4ImPF6 and up to ca. 30 μm in size for C8ImPF6). The AFM image showed that the plate thickness is very thin to be in the range of 10–50 nm (approximately 10 nm for the sample in Figure 1c).

The FE-SEM images indicated that the products are mainly Au plates with regular shapes (equilateral triangular, hexagonal, and truncated triangular shapes), coexisting with a few polyhedral particles with submicrometer dimensions (Figures 2a and 2b). The FE-SEM images also confirmed some of Au plates with

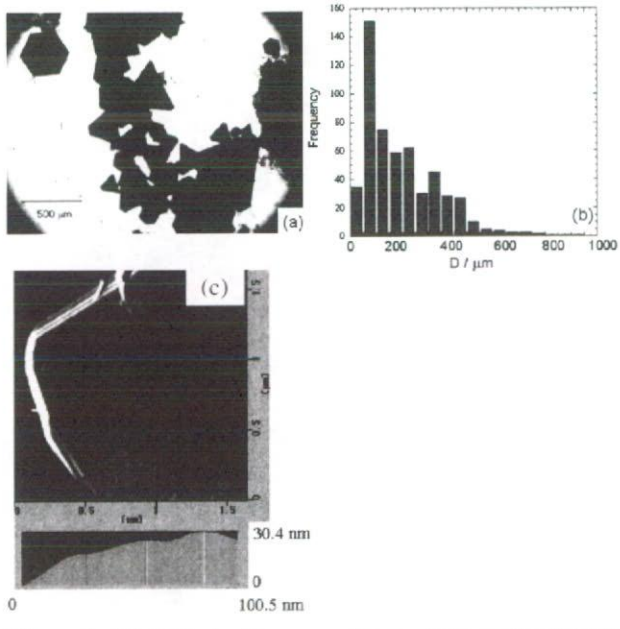

Figure 1. (a) Optical microscopy image of Au plates through thermal decomposition of $HAuCl_4$ in mixed ionic liquids of C4ImPF6 and C8ImPF6. (b) The size histogram of Au plates, and (c) the cross-sectional profile along the line of three layers of Au plates in the deflection AFM image.

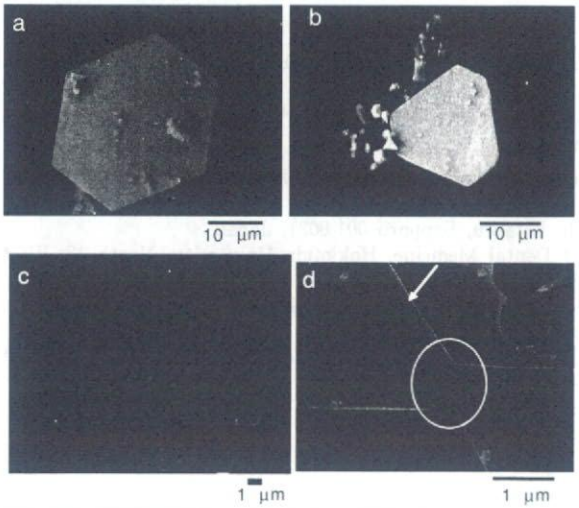

Figure 2. FE-SEM images of gold plates obtained by thermal decomposition of $HAuCl_4$ in the two-component ionic liquids of C4ImPF6 and C8ImPF6. (a), (b) Drops of ethanol dispersion of nanoplates were deposited on carbon tape. (c), (d) Samples were washed over a Pt-coated membrane filter.

very thin thickness from the transparent image (Figure 2c).[11] Energy-dispersive X-ray (EDX) analysis demonstrated that the resulting plate-like materials are composed of Au metals (Figure S1).[11] The SEM image shows lateral faces of triangular Au plates that are not perpendicular to the substrate (as shown in an arrow in Figure 2d). It has been reported that Au plates are primarily dominated by {111} facets.[9] It appears that Au plates are dominated by {111} as flat nanocrystals, probably truncated by {111} faces or {100} faces. It is worth noting that Au plates also could attach to other surface of Au plates, resulting in the rearrangement of faces of Au plates (a white circle in Figure 2d).

The ionic liquid molecules adsorbed on the Au plates were examined by surface-assisted laser desorption/ionization-mass spectrometry(SALDI-MS). The SALDI-MS analysis indicates that $C4Im^+$ with shorter alkyl chain lengths has the higher ion intensities than that of $C8Im^+$ in the mass spectrum, and the relative intensity of $C4Im^+$ (m/z 139) to $C8Im^+$ (m/z 195) was about 2 (Figure 3), suggesting that the preferential adsorption of C4ImPF6 on {111} facets of Au plates occurs during the plate growth. The stabilized effect of {111} face of Au plates in the mixed ionic liquid may be favorable to produce the extremely large size Au plates, compared to the single adsorbed layer of the ionic liquid. One minor peak at m/z 83 is attributed to a fragment ion after loss of an alkyl chain.

It should be noted that the thermal decomposition of $HAuCl_4$ in ionic liquids at high temperatures is an important parameter in producing Au plates in the ionic liquid. For example, we performed the reduction of $HAuCl_4$ in C4ImPF6 via photochemical reduction or hydrazine reduction at room temperature, but Au microplates were not formed in these routes. The photochemical reduction yielded spherical nanoparticles as main products, coexisting few rod and triangular nanoparticles, while hydrazine reduction produced Au aggregates of spherical particles (Figure S2).[11] In addition, our experiments showed if the solution of $HAuCl_4$ in the mixed ionic liquid was heated by microwave heating (300 W), Au plates with several ten

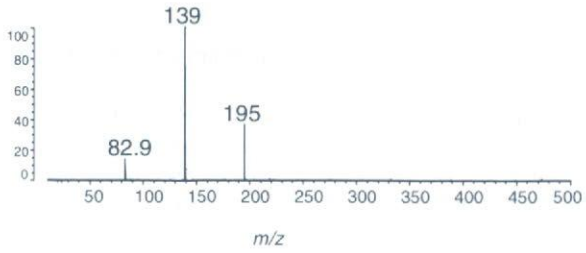

Figure 3. SALDI-TOF mass spectra obtained from the adsorbed ionic liquids (C4ImPF6 and C8ImPF6) on the Au plates in a positive mode.

micrometer-scale size were formed rapidly within five minutes. The slow reduction of gold precursors by a thermal heating may contribute to a slow rate of the plate growth and hence the formation of submillimeter-sized Au plates.

In conclusion, submillimeter-sized Au plates have been successfully prepared by the simple thermal decomposition of $HAuCl_4$ in two-component ionic liquids of C4ImPF6 and C8ImPF6. The present route is very simple and has high-yield production of Au plates. It can be estimated that this method can be extended to the fabrication of other metal plates in ionic liquids.

This work was supported by the CREST of Japan Science and Technology Corporation (JST) for Scientific Research, and in part by the Grant-in-Aid for Scientific Research (No. 17655059, No. 18710102, No. 18310069, and No. 19350045) from the Monbukagaku-shou (JSPS), Japan.

References and Notes

1 G. Schmid, *Nanoparticles: From Theory to Application*, Wiley-VCH Velag HmbH & Co. KGaA, Weingeim, Germany, **2004**.
2 M. Maillard, S. Giorgio, M.-P. Pileni, *Adv. Mater.* **2002**, *14*, 1084.
3 B. Nikoobakht, M. A. El-Sayed, *Chem. Mater.* **2003**, *15*, 1957.
4 Y. Niidome, K. Nishioka, H. Kawasaki, S. Yamada, *Chem. Commun.* **2003**, 2376.
5 J. Chen, B. J. Wiley, Y. Xia, *Langmuir* **2007**, *23*, 4120.
6 H. Kawasaki, M. Uota, T. Yoshimura, D. Fujikawa, G. Sakai, M. Annaka, T. Kijima, *Langmuir* **2005**, *21*, 11468.
7 H. Kawasaki, K. Nishimura, R. Arakawa, *J. Phys. Chem. C* **2007**, *111*, 2683.
8 M. Wirtz, C. R. Martin, *Adv. Mater.* **2003**, *15*, 455.
9 a) M. Tsuji, M. Hashimoto, Y. Nishizawa, T. Tsuji, *Chem. Lett.* **2003**, *32*, 1114. b) L. Wang, X. Chen, J. Zhan, Z. Sui, J. Zhao, Z. Sun, *Chem. Lett.* **2004**, *33*, 720. c) X. Sun, S. Dong, E. Wang, *Langmuir* **2005**, *21*, 4710. d) D. Wang, T. Imae, *Chem. Lett.* **2006**, *35*, 1152. e) X. Liu, N. Wu, B. H. Wunsch, R. J. Barsotti Jr, F. Stellacci, *Small* **2006**, *2*, 1046. f) J. Xie, J. Y. Lee, D. I. C. Wang, Y. P. Ting, *Small* **2007**, *3*, 672. g) M. Tsuji, M. Hashimoto, Y. Nishizawa, M. Kubokawa, T. Tsuji, *Chem. Eur. J.* **2005**, *11*, 440.
10 Z. Li, Z. Liu, J. Zhang, B. Han, J. Du, Y. Gao, T. Jiang, *J. Phys. Chem. B* **2005**, *109*, 14445.
11 Supporting Information is available on the CSJ-Journal website; http://www.csj.jp/journals/chem-lett/.

Published on the web (Advance View) July 14, 2007; doi:10.1246/cl.2007.1038

Dental Materials Journal 26(2): 268−273, 2007

X-ray Absorption Fine Structure (XAFS) Analysis of Titanium-implanted Soft Tissue

Motohiro UO[1], Kiyotaka ASAKURA[2], Atsuro YOKOYAMA[3], Makoto ISHIKAWA[4], Kazuchika TAMURA[5], Yasunori TOTSUKA[5], Tsukasa AKASAKA[1] and Fumio WATARI[1]

[1]Department of Biomedical Materials and Engineering, Graduate School of Dental Medicine, Hokkaido University, North 13, West 7, Kita-ku, Sapporo 060-8586, Japan
[2]Catalyst Research Center, Hokkaido University, North 21, West 10, Kita-ku, Sapporo 001-0021, Japan
[3]Department of Oral Functional Prosthodontics, Graduate School of Dental Medicine, Hokkaido University, North 13, West 7, Kita-ku, Sapporo 060-8586, Japan
[4]Department of Oral Diagnosis and Oral Medicine, Graduate School of Dental Medicine, Hokkaido University, North 13, West 7, Kita-ku, Sapporo 060-8586, Japan
[5]Department of Oral and Maxillofacial Surgery, Graduate School of Dental Medicine, Hokkaido University, North 13, West 7, Kita-ku, Sapporo 060-8586, Japan
Corresponding author, Motohiro UO; E-mail: uo@den.hokudai.ac.jp

Received September 15, 2006 /Accepted December 1, 2006

Tissues contacting Ti dental implants were subjected to X-ray absorption fine structure (XAFS) analysis to examine the chemical state of Ti transferred from the placed implant into the surrounding tissue. Nine tissues that contacted pure Ti cover screws for several months were excised in a second surgery whereby healing abutments were set. Six tissues that surrounded implants retrieved due to their failure were also excised. Ti distributions in the excised specimens were confirmed by X-ray scanning analytical microscopy (XSAM), and the specimens were subjected to fluorescence XAFS analysis to determine the chemical states of the low concentrations of Ti in the tissues surrounding Ti dental implants. Ti mostly existed in the metallic state and was considered to be debris derived from the abrasion of implant pieces during implant surgery. Oxidized forms of Ti, such as anatase and rutile, were also detected in a few specimens—and existed in either a pure state or mixed state with metallic Ti. It was concluded that the existence of Ti in the tissue did not cause implant failure. Moreover, the usefulness of XAFS for analysis of the chemical states of rarely contained elements in biological tissue was demonstrated.

Keywords: X-ray absorption fine structure (XAFS), Titanium, Implant

INTRODUCTION

Metallic materials play an important role as medical and dental implants[1]. Indeed, base metal alloys (e.g., stainless steel, cobalt-chromium alloys, and titanium alloys) are widely used as major medical and dental materials for applications that require high mechanical strength. However, these base metal alloys contain metallic elements with low biocompatibility such as nickel and chromium, and erosion and mechanical wear of metal implants placed in the human body have been reported to be associated with localized and systemic problems[2-6].

Titanium (Ti) is one of the most chemically stable and biocompatible metals. Further, it induces osseointegration (direct bonding between bone and implant) and bone formation—both of which are important features for implants. However, even Ti erodes into the surrounding bone[7-9]. Elemental distribution imaging using fluorescent X-rays—by virtue of its high sensitivity and low damage to specimens—has been employed to investigate heavy elements rarely contained in biological specimens[10-13]. However, the chemical states of eroded metallic elements in the human body have not been reported because currently available conventional methods are merely able to detect seemingly unalarming, low concentrations—which are nonetheless significant enough to be assessed for biocompatibility.

X-ray absorption fine structure (XAFS) analysis is a useful method to reveal the chemical states of target elements. In particular, its use of synchrotron radiation makes it possible to analyze the state of eroded metal in the human body at low concentrations of around 1 to 100 ppm by using fluorescence XAFS[14,15]. In a previous study, we applied fluorescence XAFS to the analysis of human soft tissue in contact with Ti dental implants, and the chemical state of Ti in two oral mucosa specimens with low concentrations of Ti could be analyzed[16]. In this study, 15 specimens from Ti dental implant-contacting tissues were analyzed by fluorescence XAFS to examine the chemical state of Ti transferred from the placed implant into the surrounding tissue.

MATERIALS AND METHODS

Tissue specimens

Fifteen oral mucosa specimens excised from nine patients through implant surgery were subjected to XAFS analysis. During dental implant surgery, fixtures of Brånemark® Mark III implants were inserted into the jaw bone. Each fixture was covered

with a cover screw, and then both fixture and cover screw were submerged under the mucosa in the first surgery. Both the fixture and cover screw consisted of commercially pure Ti with machined surface.

Nine tissues that contacted the Ti cover were excised in a second surgery whereby healing abutments were set. These tissues had closely contacted the pure Ti for several months and were available as a result of the ordinary implantation process without a need for excess surgery. Six tissues that surrounded the tissues of implants retrieved due to their failure were also excised. The excised specimens were freeze-dried and subjected to XSAM and XAFS analyses. This study was carried out with the permission of the Ethical Committee of the Graduate School of Dental Medicine of Hokkaido University.

XSAM analylsis

Ti and sulfur (S) distributions in the specimens were confirmed with an X-ray scanning analytical microscope (XSAM; XGT-2000V, Horiba). S was homogeneously contained in the specimens; therefore, S distribution images included the whole specimen. XSAM elemental distribution images were obtained with 50 scans (scan speed was 3,000 seconds per scan), and incident X-ray was obtained under the conditions of 50 kV, 1 mA. Resolution of XSAM was about 100 μm. Specimens that showed Ti localization by XSAM analysis were used for a subsequent XAFS analysis.

In a previous report[13] which also used XSAM, we observed clear Ni dissolution in Ni wire (99.9%, ø1 mm × 10 mm)-implanted rat subcutaneous tissue. This tissue showed severe inflammatory responses such as cell necrosis, macrophage migration, and blood vessel dilation around the area with dissolved Ni[13]. On this basis, it was also subjected to XAFS analysis as a negative control.

XAFS analysis

The XAFS spectra were measured at BL-9A of the Photon Factory, Institute of Materials Structure Science, High Energy Accelerator Organization (KEK-PF). Electron storage ring was operated at 2.5 GeV with 300-500 mA. Synchrotron radiation was monochromatized with a Si(111) double-crystal monochromator. Incident X-ray was focused using two bent conical mirrors into a beam 1 mm in diameter, and the specific area of the specimen where Ti was enriched was irradiated. Higher harmonics were removed using a total reflection mirror.

As for the X-ray absorption near edge structure (XANES) spectra of Ti K-edge and Ni K-edge, they were measured in a fluorescent mode using a multi-element solid-state detector (SSD; Camberra, 19 elements). I_0 signals were monitored using an N_2-filled ionization chamber. Ti foil (99.6%, Nilaco, Japan), $Ni(NO_3)_2$, and $Ni(OH)_2$ (reagent grade, Wako, Japan) were used as the standards for XAFS analysis. XANES spectra of TiO_2 (anatase and rutile) were taken from the report of Asakura *et al.*[17].

RESULTS

Table 1 shows the results of XAFS analysis of 15 specimens. Specimen Nos. 1 to 9 were derived from the oral mucosae in contact with the pure Ti cover screws through the second ordinary surgery. Specimen Nos. 10 to 15 were derived from the tissues surrounding retrieved implants. The chemical state of Ti was estimated by comparing the XANES spectra to those of reference compounds. Metallic Ti was mostly suggested; however, other states were also detected.

Figure 1 shows the typical S and Ti distribution images of four oral mucosae (numbers 1, 2, 4, and 7 in Table 1) with XSAM. The S distribution image shows the shape of the specimens. In these specimens, Ti was localized in spots, except in No. 2, suggesting the existence of particle-like materials consisting of Ti. In specimen No. 2, Ti was homogeneously distributed in parts of the specimen. Parts indicated by arrows in the Ti distribution images show the areas employed for subsequent XAFS analysis.

Figure 2 shows the Ti K-edge XANES spectra of specimen No. 1 (arrow in Fig. 1) and Ti foil as the standard. The spectrum of specimen No. 1 was quite

Table 1 Ti K-edge absorption and chemical state of Ti contained in Ti implant (Brånemark® Mark III)-surrounding tissues using fluorescence XAFS analysis. (Nos. 1 to 9: in contact with pure Ti cover screws (machined surface) of successful implants; Nos. 10 to 15: excised from retrieved implants with machined surface.)

Specimen	Chemical state of Ti	Patient (Gender)
1	Metal	A (Female)
2	Anatase	B (Female)
3	Metal (80%) + Anatase (20%)	B (Female)
4	Metal (80%) + Anatase (20%)	C (Female)
5	Metal	D (Female)
6	Metal	D (Female)
7	Metal (80%) + Rutile (20%)	E (Male)
8	Metal	E (Male)
9	Metal	F (Male)
10	Metal (85%) + Anatase (15%)	E (Male)
11	Metal	E (Male)
12	Metal	G (Female)
13	Metal	G (Female)
14	Metal	G (Female)
15	Metal	G (Female)

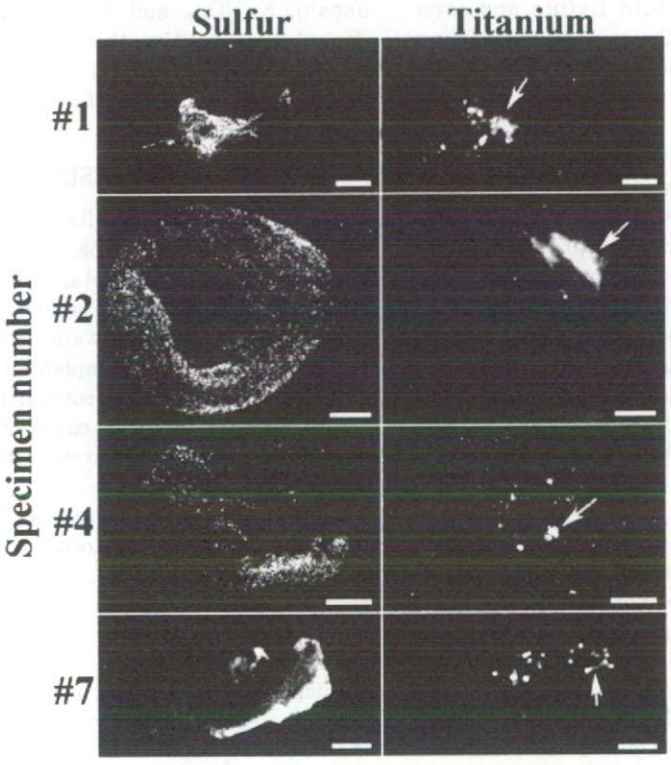

Fig. 1 Elemental distribution images of typical Ti implant-surrounding tissues using XSAM (bars in images show 1 mm).

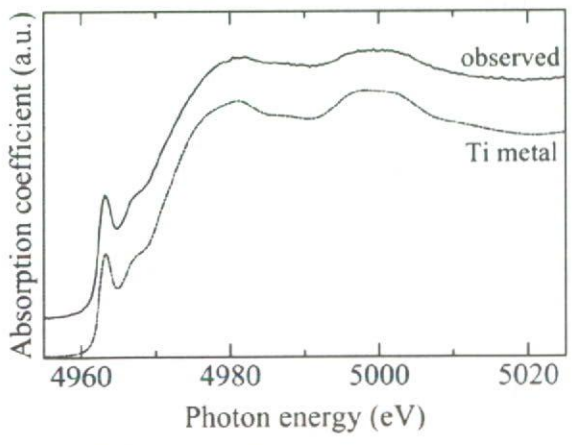

Fig. 2 Ti K-edge XANES spectra of specimen No. 1 and Ti foil.

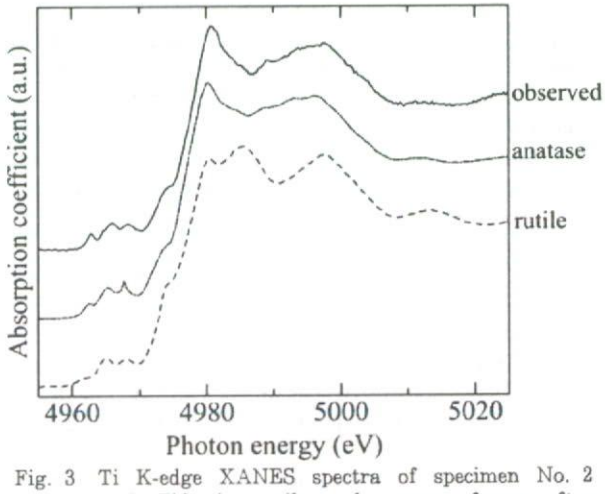

Fig. 3 Ti K-edge XANES spectra of specimen No. 2 and TiO_2 in rutile and anatase forms after Asakura *et al.*[17].

close to that of Ti foil. Therefore, the localized Ti in specimen No. 1 was estimated to be in the metallic state. Figure 3 shows the spectra of specimen No. 2 (as previously reported[16]) and TiO_2 (anatase and rutile[17]). The spectrum of specimen No. 2 was close to that of anatase. Therefore, the localized Ti in specimen No. 2 was considered to be anatase. Figure 4 shows the XANES spectrum of specimen No. 4. The observed XANES spectrum was similar to that of metallic Ti, but fit well with a mixture of metallic Ti and anatase. A mixture of about 80% metal and 20% anatase well described the observed spectrum. Figure 5 shows the XANES spectrum of specimen No. 7. Like specimen No. 4, the Ti distribution and the observed XANES spectrum indicated the presence of metallic Ti, but the peak marked by the arrow in the observed spectrum did not exist in the spectrum of metallic Ti. On the overall, the spectrum fit well

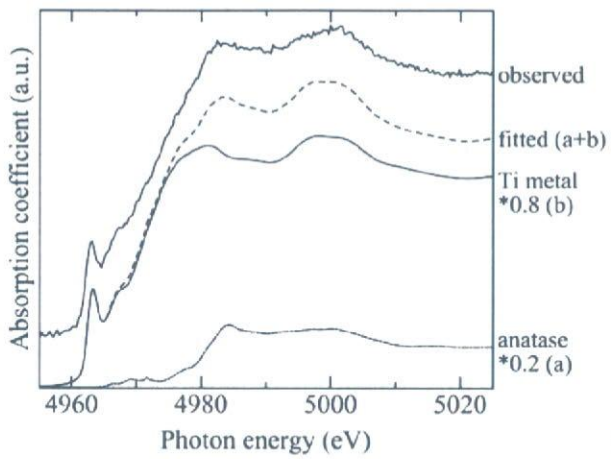

Fig. 4 Ti K-edge XANES spectrum of specimen No. 4 and a curve fitting those of metallic Ti and TiO_2 in anatase.

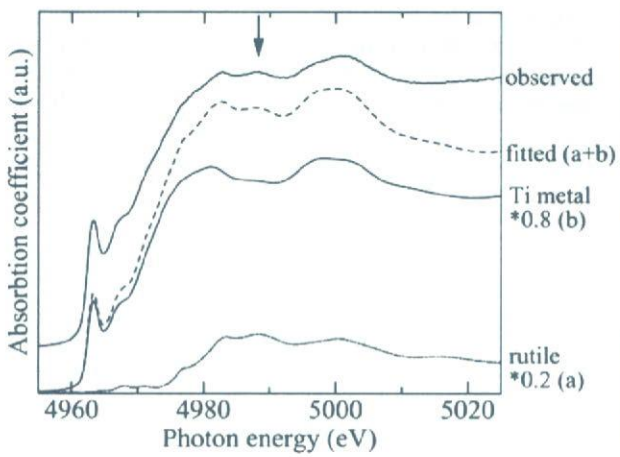

Fig. 5 Ti K-edge XANES spectrum of specimen No. 7 and a curve fitting those of metallic Ti and TiO_2 in rutile.

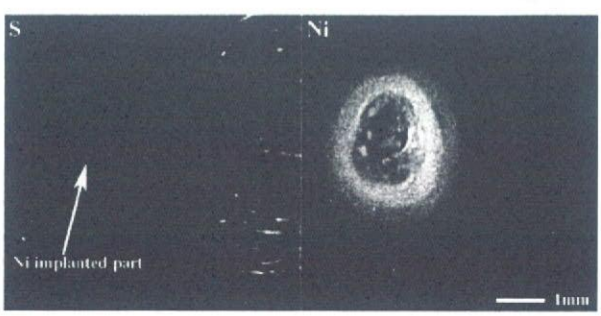

Fig. 6 Elemental distribution images of Ni-implanted rat subcutaneous tissue using XSAM.

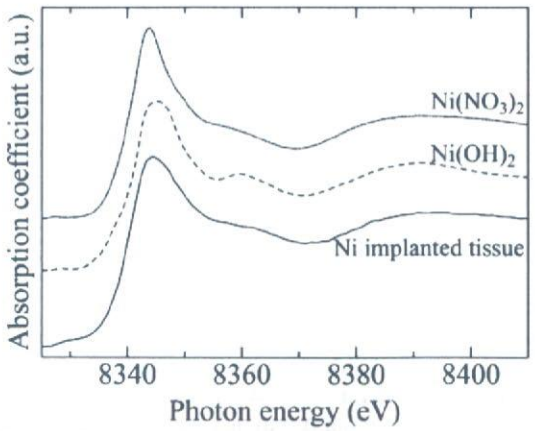

Fig. 7 Ni K-edge XANES spectrum of an Ni-implanted rat specimen and those of $Ni(NO_3)_2$ and $Ni(OH)_2$.

with a mixture of metallic Ti (80%) and rutile (20%).

Figure 6 shows the Ni and S distribution images of Ni-implanted rat subcutaneous tissue obtained by XSAM. Ni dissolution was clearly observed, and the area with dissolved Ni extended up to about 1.5 mm from the position of the implant surface. The Ni K-edge XANES spectrum of the dissolved Ni in the abovementioned tissue and those of the standard Ni compounds are shown in Fig. 7. The spectrum of Ni dissolved in the rat soft tissue was close to that of $Ni(OH)_2$ and identical to that of $Ni(NO_3)_2$.

DISCUSSION

Despite the high chemical stability and biocompatibility of pure Ti dental implants, Ti was detected in tissues surrounding the implants. We analyzed 15 Ti-containing oral mucosae obtained from patients who had Ti dental implants, and the chemical state of Ti was estimated with fluorescence XAFS analysis. As shown in Table 1, 10 of the specimens showed the existence of metallic Ti. Further, as shown for specimen No. 1 in Fig. 1, the Ti distribution images of these specimens suggested the existence of particulate Ti. Putting these results together, it could be said that Ti in those tissues consisted of metallic Ti particles.

During the first implant surgery, the dental implant fixture was covered with a cover screw. The surface of placed implants in this study were machined but not polished. Therefore, abrasion between the inner surface of the fixture and the outer surface of the cover screw appeared to generate Ti debris. Wear debris generation from metal-on-metal hip joints *in vivo* has been reported[18]. Therefore, the origin of Ti particles in these specimens was attributed to abrasion-generated debris during implant surgery. In the XSAM observation, Ca distributions were also measured. These images

were similar to S distribution images and there were no relations to Ti distribution images.

In one specimen (No. 2), Ti existed as anatase. In a few other specimens (Nos. 3, 4, 7, and 10), mixed states of metallic Ti and titanium dioxide (anatase or rutile) were observed. As shown for specimen Nos. 4 and 7 in Fig. 1, the Ti distribution images of these specimens suggested the existence of particulate Ti. Moreover, even in the mixed state, metallic Ti debris constituted a greater portion in these specimens with the existence of a small amount of anatase. One speculation for the origin of these oxides was that Ti eroded and dissolved into the surrounding tissue and might have oxidized and localized. Alternatively, the TiO_2 layer on the implant surface was abraded and transferred into the tissue. Anatase is the low-temperature form of titanium dioxide. As such, its presence as the oxidized state of dissolved Ti ions was a reasonable and acceptable one. Moreover, anatase formation from dissolved Ti can be corroborated from the many reports on the corrosion behavior of Ti[19-28]. However, the existence of rutile was a curious one because it is a high-temperature form of titanium dioxide. One possible source was the abrasion of Ti oxide film on the implant material. In this case, the state of Ti would depend on the history and background of the material before surgery. Removed cover screws (specimen Nos. 1 – 9) and extracted implants (specimen Nos. 10 – 15) showed a metallic surface, whereby no corrosion was observed in visual inspection. On this note, the relationship between the chemical state of Ti in the surrounding tissues and the surface condition of implanted Ti was not fully clarified and thoroughly determined in this study. Additional study is thus necessary to confirm the transfer process of Ti.

The implants of six patients, specimen Nos. 1 to 9, were stable despite the transfer of Ti into the surrounding tissue. As shown in Table 1, the same chemical states were found for both successful and failed implants. In other words, implant failure could not be ascribed to the spread of Ti in the tissue. As for the explanation to this dual success/failure condition of implants, it could be attributed to two factors: Ti in the surrounding tissue was in a chemically stable state (such as metallic Ti and TiO_2), and that it was localized in a narrow area around the tissue in contact with the implant *versus* widespread dissemination of Ti debris from the implant.

In contrast to Ti, dissolved Ni spread homogeneously in the soft tissue and existed in an aquo complex as shown in Figs. 6 and 7. In the specimen shown in Fig. 6, severe inflammatory responses such as cell necrosis, macrophage migration, and blood vessel dilation were observed in the area with dissolved Ni[13]. Figure 7 then suggested that the Ni species present in rat soft tissue was surrounded by water to form an aquo complex. The Ni aquo complex would be diffusible and reactive in the soft tissue. As a result, the toxicity of Ni ions caused severe inflammatory responses in the tissue. At this juncture, it is worth highlighting that differences in the chemical state between Ti and Ni in the soft tissue would affect the diffusibility and toxicity of dissolved species in the tissue. Therefore, analysis of the chemical state of a metal species in soft tissue was considered to be useful in evaluating its biocompatibility.

Concentrations of released metal ions and small debris in the tissues surrounding medical and dental implants are usually quite low. Therefore, such tissues require high-intensity incident X-rays (e.g., synchrotron radiation) coupled with high sensitivity (e.g., X-ray fluorescence or XAFS analysis). For example, Ektessabi *et al.*[29] detected metal ions released from a failed hip replacement system by synchrotron radiation-excited X-ray fluorescence spectroscopy; however, their chemical states were still unknown. In this study, we employed fluorescence XAFS, which provided higher sensitivity than ordinary transmission XAFS with synchrotron radiation because of low background in the spectrum[30]. In this manner, the chemical states of low concentrations of metal elements in tissues were successfully analyzed using fluorescence XAFS method.

CONCLUSIONS

In this study, we successfully estimated the chemical states of low concentrations of Ti in tissues surrounding Ti dental implants using fluorescence XAFS. Ti existed mostly in the metallic state and was considered to be debris derived from the abrasion of implant pieces during implant surgery. Oxidized Ti forms, such as anatase and rutile, were also detected in a few specimens – they existed in either a pure state or mixed state with metallic Ti. As for Ti that transferred from the dental implants into the surrounding tissues, it existed in chemically stable states (such as metallic Ti and titanium dioxide) and localized near the implants. The same chemical states were found for both successful and failed implants, and always close to the implant surface. Therefore, failure could not be ascribed to the spreading of Ti in the tissue. In this work, we demonstrated the usefulness of using XAFS for the analysis of the chemical states of rarely contained metallic elements in tissues surrounding metallic implants.

ACKNOWLEDGEMENTS

The XAFS measurements were done with the approval of the Photon Factory Advisory Committee

(Proposal No. 2004G084, 2006G199). This work was also supported by a Grant-in-Aid for Scientific Research (B), No. 18390509, from the Ministry of Education, Culture, Sports, Science and Technology, Japan.

REFERENCES

1) McNamara A, Williams DF. The response to the intramuscular implantation of pure metal. Biomaterials 1981; 2:33-40.
2) McNamara A, Williams DF. Scanning electron microscopy of the metal-tissue interface. I. Fixation methods and interpretation of results. Biomaterials 1982; 3:160-164.
3) McNamara A, Williams DF. Scanning electron microscopy of the metal-tissue interface. II. Observations with lead, copper, nickel, aluminum, and cobalt. Biomaterials 1982; 3:165-176.
4) Schliephake H, Reiss G, Urban R, Neukam FW, Guckel S. Metal release from titanium fixtures during placement in the mandible: An experimental study. Int J Oral Maxillofac Implants 1993; 8 502-511.
5) Hallab NJ, Skipor A, Jacobs JJ. Interfacial kinetics of titanium- and cobalt-based implant alloys in human serum: Metal release and biofilm formation. J Biomed Mater Res 2003; 65A:311-318.
6) Kasai Y, Iida R, Uchida A. Metal concentration in the serum and hair of patients with titanium alloy spinal implants. Spine 2003; 28:1320-1326.
7) Ferrari F, Miotello A, Pavloski L, Galvanetto E, Moschini G, Galassini S, Passi P, Bogdanovic S, Fazinic S, Jaksic M, Valkovic V. Metal-ion release from titanium and TiN coated implants in rat bone. Nucl Instr and Meth B 1993; B79:421-423.
8) Ektessabi AM, Otsuka T, Tsuboi Y, Yokoyama K, Albrektsson T. Sennerby L, Johansson C. Application of micro beam PIXE to detection of titanium ion release from dental and orthopaedic implants. Int J PIXE 1994; 4:81-91.
9) Gorustovich A, Rosenbusch M, Guglielmotti MB. Characterization of bone around titanium implants and bioactive glass particles: an experimental study in rats. Int J Oral Maxillofac Implants 2002; 17:644-650.
10) Kitamura N, Ektessabi AM. XAFS in a single macrophage cell. J Synchrotron Rad 2001; 8:981-983.
11) Kagoshima Y, Takai K, Ibuki T, Yokoyama Y, Hashida T, Yokoyama K, Takeda S, Urakawa M, Miyamoto N, Tsusaka Y, Matsui J, Aino M. Scanning hard X-ray microscope with tantalum phase zone plate at the Hyogo-BL (BL24XU) of SPring-8. Nucl. Instrum & Methods A 2001; 467-468:872-876.
12) Dillon CT, Kennedy BJ, Lay PA, Lai B, Cai Z, Stampfl APJ, Ilinski P, Legnini DG, Maser J, Rodrigues W, Shea-McCarthy G, Cholewa M. Implementation of X-ray microscopy and micro-XANES analysis for investigations of the cellular uptake and cellular metabolism of transition metals. J Phys IV 2003; 104:293-296.
13) Uo M, Tanaka M, Watari F. Quantitative analysis of biological specimens by X-ray scanning analytical microscopy. J Biomed Mater Res B Appl Biomater 2004; 70B:146-151.
14) Nomura M. Dead-time correction of a multi-element SSD for fluorescent XAFS. J Synchrotron Rad 1998; 5:851-853.
15) Chun WJ, Tanizawa Y, Shido T, Iwasawa Y, Nomura M, Asakura K. Development of an in situ polarization-dependent total-reflection fluorescence XAFS measurement system. J Synchrotron Rad 2001; 8:168-172.
16) Uo M, Asakura K, Yokoyama A, Tamura K, Totsuka Y, Akasaka T, Watari F. Analysis of titanium dental implants surrounding soft tissue using X-ray absorption fine structure (XAFS) analysis. Chem Lett 2005; 34:776-777.
17) Asakura K, Inukai J, Iwasawa Y. Structure of one atomic layer titanium oxide on silica and its palladium-mediated restructuring. J Phys Chem 1992; 96:829-834.
18) Büscher R, Täger G, Dudzinski W, Gleising B, Wimmer MA, Fischer A. Subsurface microstructure of metal-on-metal hip joints and its relationship to wear particle generation. J Biomed Mater Res Part B 2005; 72B:206-214.
19) Khan MA, Williams RL, Williams DF. *In-vitro* corrosion and wear of titanium alloys in the biological environment. Biomaterials 1996; 17:2117-2126.
20) Cai Z, Nakajima H, Woldu M, Berglund A, Bergman M, Okabe T. *In vitro* corrosion resistance of titanium made using different fabrication methods. Biomaterials 1999; 20:183-190.
21) Grosgogeat B, Reclaru L, Lissac M, Dalard F. Measurement and evaluation of galvanic corrosion between titanium/Ti6Al4V implants and dental alloys by electrochemical techniques and auger spectrometry. Biomaterials 1999; 20:933-941.
22) Nakagawa M, Matsuya S, Udoh K. Corrosion behavior of pure titanium and titanium alloys in fluoride containing solutions. Dent Mater J 2001; 20:305-314.
23) Hanawa T, Hiromoto S, Asami K, Okuno O, Asaoka K. Surface oxide films on titanium alloys regenerated in Hanks' solution. Mater Trans 2002; 43:3000-3004.
24) Cai Z, Shafer T, Watanabe I, Nunn ME, Okabe T. Electrochemical characterization of cast titanium alloys. Biomaterials 2003; 24:213-218.
25) Takahashi M, Kikuchi M, Takada Y, Okuno O, Okabe T. Corrosion behavior and microstructures of experimental Ti-Au alloys. Dent Mater J 2004; 23:109-116.
26) Takemoto S, Hattori M, Yoshinari M, Kawada E, Asami K, Oda Y. Corrosion behavior and surface characterization of Ti-20Cr alloy in a solution containing fluoride. Dent Mater J 2004; 23:379-386.
27) Takada Y, Okuno O. Corrosion characteristics of α-Ti and Ti_2Cu composing Ti-Cu alloys. Dent Mater J 2005; 25:610-616.
28) Matono Y, Nakagawa M, Matsuya S, Ishikawa K, Terada Y. Corrosion behavior of pure titanium and titanium alloys in various concentrations of Acidulated Phosphate Fluoride (APF) solutions. Dent Mater J 2006; 25:104-112.
29) Ektessabi AM, Rokkum M, Johansson C, Albrektsson T, Sennerby L, Saisho H, Honda S. Application of synchrotron radiation in investigation of metal-ion release from a hip replacement prosthesis. J Synchrotron Rad 1998; 5:1136-1138.
30) Asakura K. Fluorescent XAFS. Shokubai 2000; 42: 328-332.

Fullerenes, Nanotubes, and Carbon Nanostructures, 15: 303–309, 2007

ISSN 1536-383X print/1536-4046 online
DOI: 10.1080/15363830701423773

Taylor & Francis
Taylor & Francis Group

The Purity and Thermal Stability in Air of Metal-Encapsulating Carbon Nanocapsules (MECNCs)

Motohiro Uo, Hanako Kachi, Tsukasa Akasaka, and Fumio Watari
Department of Biomedical Materials and Engineering, Graduate School of Dentistry, Hokkaido University, Sapporo, Japan

Yoshinori Sato, Kenichi Motomiya, and Kazuyuki Tohji
Graduate School of Environmental Studies, Tohoku University, Sendai, Japan

Abstract: Rare earth elements (Y, La, Ce, Nd, Gd and Dy) encapsulated by carbon nanocapsules (CNCs) were synthesized and their purity and air oxidation stability were estimated. The purity was estimated as the rare earth carbide content. Gd- and Dy-encapsulating CNCs had higher than 30 wt% and others 15 to 20 wt%. Encapsulated rare earth carbide was oxidized by heating in air at 400°C or higher. This suggested oxidation damage to the graphene capsules of CNCs.

Keywords: Metal encapsulating carbon nanocapsules, rare earth, carbide, purity, thermal stability

INTRODUCTION

Metal-encapsulating carbon nanocapsules (MECNCs) are several tens of nanometers in diameter and consist of a graphene sheet structure encapsulating a metallic carbide. MECNCs have a surface covered by a graphene sheet, so they have quite high chemical stability (1–10). In the capsule synthesized

Received 19 September 2006, Accepted 15 December 2006
Address correspondence to Motohiro Uo, Department of Biomedical Materials and Engineering, Graduate School of Dentistry, Hokkaido University, 060-8586 Sapporo, Japan. E-mail: uo@den.hokudai.ac.jp

by using a direct current arc-discharge method with a lanthanide-loading graphite anode, lanthanide is usually encapsulated as a carbide. The formation of MECNCs was suggested as the segregation of excess carbon composition from the metal carbide droplets while they are cooling (4). Metallofullerenes have been studied as contrast agents in X-ray or magnetic resonance imaging (11, 12).

MECNCs also contain metallic elements in the graphite capsule, but the size of the capsule and the amount of encapsulated metallic elements are a hundred times larger than metallofullerenes. In addition, the graphene capsules have high chemical stability and the encapsulated metals are stable in air, water and concentrated sulfuric acid, and these features will provide higher imaging and tracing efficiencies as contrast agents or tracers as the authors have reported the low cytotoxicity of MECNCs (13). In the application of MECNCs, their purity and the chemical stability of the graphene capsules must be estimated.

EXPERIMENTAL PROCEDURES

MECNCs were synthesized by a direct current arc-discharge between a pure graphite cathode and a metal-loaded graphite anode in a helium atmosphere. A pure graphite rod (purity 99.9%, Wakomu Denso Co., Japan) and a graphite rod loaded with Y_2O_3, La_2O_3, CeO_2, Nd_2O_3, Gd_2O_3 and Dy_2O_3 powder (99.9%, Wako Pure Chemical Industries, Japan) as the source of rare earth were used as the cathode and anode, respectively. The arc-discharge was carried out in helium gas at 500 Torr. A carbonaceous deposit on the cathode was corrected and the synthesis of the MECNCs was confirmed with TEM observation (TEM: Hitachi, HF-2000, Japan), energy-dispersive X-ray spectroscopy analysis (EDXS: NORAN Instruments, VANTAGE, USA) and X-ray diffraction (XRD: Rigaku, Multiflex, Japan). As-grown MECNCs, MECNCs heated at 350 to 450°C in air for 30 minutes and MECNCs heated at 450°C in vacuum (10^{-6} torr) were subjected to X-ray diffraction to estimate the crystalline state of encapsulated rare earth. Some MECNCs were heated at 800°C for 2 hours to burn out the graphene capsule and the rare earth oxide that remained was weighed. The rare earth carbide contents in as-grown MECNCs were converted from the final oxide weight and the chemical formulae of the rare earth carbides and oxides were assigned.

RESULTS AND DISCUSSION

MECNCs encapsulating Y, La, Ce, Nd, Gd and Dy were successfully synthesized. Later, those MECNCs are abbreviated as Y-CNCs. Figure 1 shows the TEM image of Ce-CNCs. We observed many MECNCs as well as

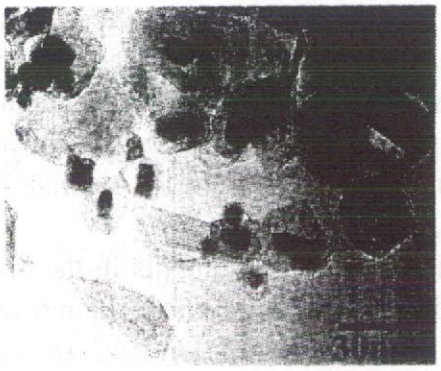

Figure 1. High magnification TEM image of MECNCs (Ce-CNCs).

non-encapsulating carbon nanocapsules. The single-crystal CeC_2 compounds were encapsulated in the multi-walled carbon layers. The fact that the CeC_2 interior was single-crystalline was confirmed by electron diffraction (9) and EDXS. The estimated rare earth carbide contents in various MECNCs are presented in Table 1. The weights of the MECNCs were mostly obtained from the rare earth carbide cores. Therefore, the carbide contents were close to the purity of the MECNCs. The purity levels of Gd- and Dy-containing CNCs were more than 30 wt% and others were less than 20 wt%. Therefore, graphite, amorphous carbon and vacant carbon nanocapsules were contained as impurities.

Figure 2(a) shows the X-ray diffraction spectra of Ce-encapsulating nanocapsules (Ce-CNCs) as grown and heated at 350 to 450°C. As-grown Ce-CNCs show diffraction peaks derived from the graphite and CeC_2. The spectrum was not changed after heating at 350°C, but CeO_2 appeared after heating at higher than 400°C. Rare earth carbides are instable in air and easily oxidized. In MECNCs, however, the graphene capsule is airtight; therefore, the rare earth carbide is isolated from the air. When heated at higher than 400°C in air, the graphene capsule was damaged by oxidation and the encapsulated CeC_2 was oxidized to CeO_2. Similarly, Y-CNCs showed peaks derived from the oxide species (Y_2O_3) after heating at 400°C

Table 1. Rare earth carbide content in raw MECNCs

MECNCs	Chemical formula of encapsulated carbide	Carbide content (wt%)
Y-CNCs	YC_2	16
La-CNCs	LaC_2	19
Ce-CNCs	CeC_2	19
Nd-CNCs	NdC_2	20
Gd-CNCs	GdC_2	35
Dy-CNCs	DyC_2	31

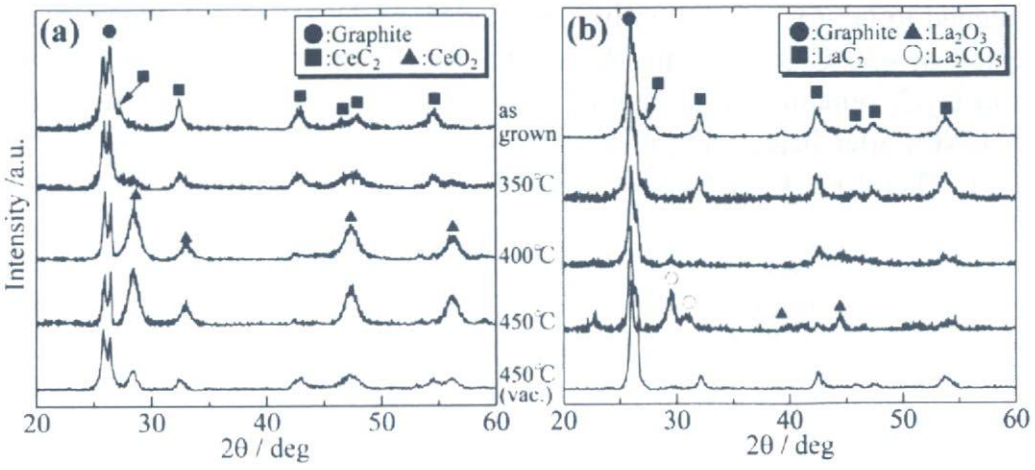

Figure 2. Changes in X-ray diffraction spectra of Ce- and La-CNCs with heat treatment.

or higher. Figure 2(b) shows the X-ray diffraction spectra of La-CNCs as grown and heated at 350 to 450°C. As-grown La-CNCs show diffraction peaks derived from the graphite and LaC_2.

After heating at 400°C, peaks of LaC_2 became weak and peaks of La_2O_3 and La_2CO_5 appeared at above 450°C. Nd-CNCs showed $Nd_2O_2CO_3$ after 450°C. These results showed that La- and Nd-CNCs were stable at lower than 350°C and that carbonate or oxicarbonate species were formed at 450°C. After heating at 450°C in vacuum, Ce-CNCs showed CeO_2 peaks, however, La-CNCs were not changed. Also, Y-CNCs and Nd-CNCs were not changed after heating at 450°C in vacuum. Then, Ce-CNCs would be less stable for heating.

Figure 3(a) shows the X-ray diffraction spectra of Gd-CNCs as grown and heated at 350 to 450°C. The peaks derived from GdC_2 remained after heating at 400°C. At 450°C, peaks assigned to GdC_2 disappeared and unclear peaks

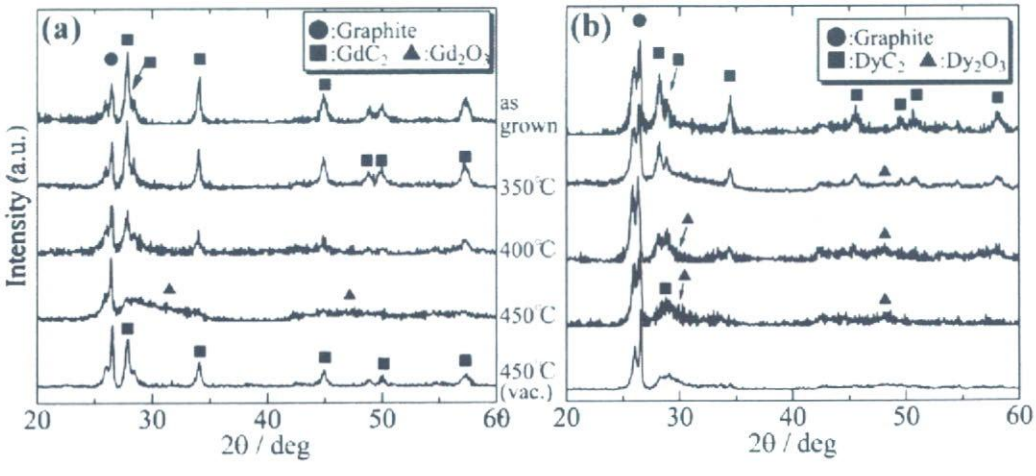

Figure 3. Changes in X-ray diffraction spectra of Dy- and Gd-CNCs with heat treatment.

assigned to Gd_2O_3 were slightly increased. Gd-CNCs was not changed after heated at 450°C in vacuum. As shown in Figure 3(b), the peaks derived from DyC_2 remained after heating at 400°C, but the peaks were broadened. Dy-CNCs after heated at 450°C in vacuum was similar to that after heated in air. Therefore, Gd-CNCs would have the highest stability for heating in air and vacuum.

Figure 4 shows the TEM images of Gd- and Dy-CNCs after heated at 450°C. Gd or Dy encapsulating CNCs (points 1 and 3 in Figure 4) were remained and large granules (points 2 and 4) were generated after heating. The compositions of each point analyzed by EDXS were tabulated in Table 2. Points 1 and 3 contain the rare earth (Gd or Dy) and C. Then, the remaining of Gd-and Dy-CNCs after heated at 450°C could be confirmed. Point 2 and 4 which were generated large granules showed high oxygen content. Those granules could be assumed that the most of MECNCs were oxidized and degraded by heating, and then encapsulated rare earth was formed oxide particles. In Y-, La-, Ce-and Nd-CNCs that showed no carbides in XRD spectra after heated at 450°C, the remained MECNCs could not observed by TEM observation. Therefore, the heating stability estimated by XRD was confirmed by TEM observation.

Oxidation treatment at around 500°C was useful for the purification of carbon nanotubes because the impurities, e.g., amorphous carbon or hydrocarbon, were burned out before nanotube oxidation. In this study, the encapsulated rare earth carbides in MECNCs were oxidized by heating at 400 to 450°C in air. Ajayan et al. suggested that both the strain at the tip and the presence of pentagons might help the initiation of the oxidation at the caps of carbon nanotubes (14).

MECNCs have tips that would contain pentagons, thus, heating in air would promote the oxidation at the tips of the graphene capsules of MECNCs and airtightness is lost. Then the encapsulated rare earth carbide is oxidized. The airtightness of the graphene capsule means that the

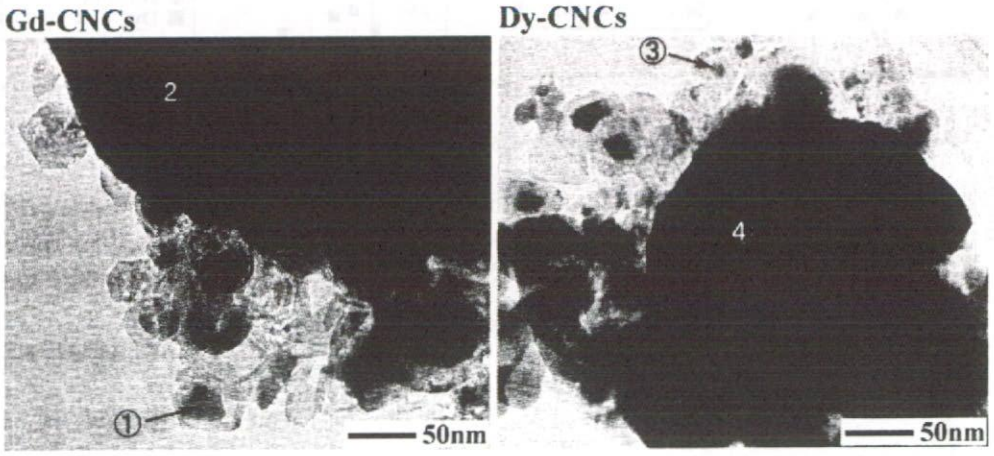

Figure 4. TEM images of Dy- and Gd-CNCs after heat treatment at 450°C.

Table 2. EDXS analysis of Gd- and Dy-CNCs after heated 450°C shown in Figure 4 (at%)

Elements analyzed point	Gd	Dy	C	O
1	7.0	—	92.4	0.6
2	10.6	—	66.1	23.3
3	—	76.9	20.9	2.2
4	—	27.5	51.9	20.6

encapsulated elements are isolated from the outside. Oxidation of encapsulated rare earth elements indicates damage to the graphene capsules and loss of their airtightness. Therefore, MECNCs heated at higher than 400°C in air lose their chemical stability, and the encapsulated elements become erosive. In other words, MECNCs are stable at lower than 350°C and the erosion of encapsulated elements is negligible. This feature is important for biomedical application as the authors have reported the low cytotoxicity of Ce-CNCs (13). In this study, various rare earth elements were encapsulated in carbon nanocapsules. Gd-CNCs had the highest purity (35 wt%) among the synthesized MECNCs and slightly better stability for heating in air up to 450°C. Concerning the Gd-CNCs, paramagnetic properties and magnetic separation were suggested (15, 16). Thus, Gd-CNCs would be favorable for biomedical and other applications.

ACKNOWLEDGMENTS

This work was supported by Research on Advanced Medical Technology in Health and Labour Sciences Research Grants from the Ministry of Health, Labour and Welfare of Japan. A part of this study was also supported by Grant-in-Aid for Scientific Research (B) No.18390509 from the Ministry of Education, Culture, Sports, Science and Technology, Japan.

REFERENCES

1. Ruoff, R.S., Lorents, D.C., Chan, B., Malhotra, R., and Subramoney, S. (1993) Single crystal metals encapsulated in carbon nanoparticles. *Science*, 259: 346.
2. Tomita, M., Saito, Y., and Hayashi, T. (1993) LaC_2 encapsulated in graphite nanoparticles. *Jpn J. Appl. Phys.*, 32: L280.
3. Yosida, Y. (1993) Synthesis of CeC_2 crystals encapsulated within gigantic super fullerenes. *Appl. Phys. Lett.*, 62: 3447.
4. Saito, Y., Yoshikawa, T., Okuda, M., Ohkohchi, M., Ando, Y., Kasuya, A., and Nishina, Y. (1993) Synthesis and electron-beam incision of carbon nanocapsules encaging YC_2. *Chem. Phys. Lett.*, 209: 72.

5. Seraphin, S., Zhou, D., Jiao, J., Withers, J.C., and Loutfy, R. (1993) Selective encapsulation of the carbides of yttrium and titanium into carbon nanoclusters. *Appl. Phys. Lett.*, 63: 2073.
6. Saito, Y., Okuda, M., Yoshikawa, T., Bandow, S., Yamamuro, S., Wakoh, K., Sumiyama, K., and Suzuki, K. (1994) Synthesis of $Sc_{15}C_{19}$ crystallites encapsulated in carbon nanocapsules by arc evaporation of Sc-C composite. *Jpn. J. Appl Phys.*, 33: L186.
7. Funasaka, H., Sugiyama, K., Yamamoto, K., and Takahashi, T. (1995) Synthesis actinide carbides encapsulated within carbon nanoparticles. *J. Appl. Phys.*, 78: 5320.
8. Pasqualini, E., Adelfang, P., and Regueiro, M.N. (1996) Carbon nanoencapsulation of uranium dicarbide. *J. Nucl. Mater.*, 231: 173.
9. Yosida, Y. (1997) A new type of ultrafine particles: rare earth dicarbide crystals encapsulated in carbon nanocages. *Physica*, 229: 301.
10. Sato, Y., Jeyadevan, B., Hatakeyama, R., Kasuya, A., and Tohji, K. (2004) Electronic properties of radial single-walled carbon nanotubes. *Chem. Phys. Lett.*, 385: 323.
11. Mikawa, M., Kato, H., Okumura, M., Narazaki, M., Kanazawa, Y., Miwa, N., and Shinohara, H. (2001) Paramagnetic water-soluble metallofullerenes having the highest relaxivity for MRI contrast agents. *Bioconjugate Chem.*, 12: 510.
12. Bolskar, R.D., Benedetto, A.F., Husebo, L.O., Price, R.E., Jackson, E.F., Wallace, S., Wilson, L.J., and Alford, M. (2003) First soluble $M@C_{60}$ derivatives provide enhanced access to metallofullerenes and permit in vivo evaluation of $Gd@C_{60}[C(COOH)_2]_{10}$ as a MRI contrast agent. *J. Am. Chem. Soc.*, 125: 5471.
13. Uo, M., Tamura, K., Sato, Y., Yokoyama, A., Watari, F., Totsuka, Y., and Tohji, K. (2005) The cytotoxicity of metal-encapsulating carbon nanocapsules. *Small*, 1: 816.
14. Ajayan, P.M., Ebbesen, T.W., Ichihashi, T., Iijima, S., Tanigaki, K., and Hiura, H. (1993) Opening carbon nanotubes with oxygen and implications for filling. *Nature*, 362: 522.
15. Majetich, S.A., Artman, J.O., McHenry, M.E., Nuhfer, N.T., and Staley, S.W. (1993) Preparation and properties of carbon-coated magnetic nanocrystallites. *Phys. Rev. B*, 48: 16845.
16. Subramoney, S., Ruoff, R.S., Lorents, D.C., Chan, B., Malhotra, R., Dyer, M.J., and Parvin, K. (1994) Magnetic separation of GdC_2 encapsulated in carbon nanoparticles. *Carbon*, 32: 507.

J Mater Sci: Mater Med (2007) 18:661–668
DOI 10.1007/s10856-007-2317-1

Mechanical properties and apatite forming ability of TiO_2 nanoparticles/high density polyethylene composite: Effect of filler content

Masami Hashimoto · Hiroaki Takadama · Mineo Mizuno · Tadashi Kokubo

Received: 23 December 2004 / Accepted: 21 October 2005

Abstract Composite materials consisting of TiO_2 nanoparticles and high-density polyethylene (HDPE), designated hereafter as TiO_2/HDPE, were prepared by a kneading and forming process. The effect of TiO_2 content on the mechanical properties and apatite forming ability of these materials was studied. Increased TiO_2 content resulted in an increase in bending strength, yield strength, Young's modulus and compressive strength (bending strength = 68 MPa, yield strength = 54 MPa, Young's modulus = 7 GPa, and compressive strength = 82 MPa) at 50 vol% TiO_2. The composite with 50 vol% TiO_2 shows a similar strength and Young's modulus to human cortical bone. The TiO_2/HDPE composites with different TiO_2 contents were soaked at 36.5 °C for up to 14 days in a simulated body fluid (SBF) whose ion concentrations were nearly equal to those of human blood plasma. The apatite forming ability, which is indicative of bioactivity, increased with TiO_2 content. Little apatite formation was observed for the TiO_2/HDPE composite with 20 vol% content. However, in the case of 40 vol% TiO_2 content and higher, the apatite layers were formed on the surface of the composites within 7 days. The most potent TiO_2 content for a bone-repairing material was 50 vol%, judging from the mechanical and biological results. This kind of bioactive material with similar mechanical properties to human cortical bone is expected to be useful as a load bearing bone substitute in areas such as the vertebra and cranium.

M. Hashimoto · H. Takadama (✉) · M. Mizuno
Japan Fine Ceramics Center, 2-4-1 Mutsuno, Atsuta-ku, Nagoya 456-8587, Japan
e-mail: masami@jfcc.or.jp

T. Kokubo
Research Institute for Science and Technology, Chubu University, 1200 Matsumoto-cho, Kasugai 487-8501, Japan

Introduction

It has been reported that some ceramics, such as Na_2O-CaO-SiO_2-P_2O_5 glasses [1], sintered hydroxyapatite [2], and glass-ceramics containing crystalline apatite and wollastonite (A-W) [3], can bond to living bone. These ceramics are already clinically used as important bone-repairing materials. Recently, it was also reported that even metals such as titanium and its alloys can bond to living bone when they have been previously subjected to alkali and heat treatment [4] or alkali, water and heat treatment [5]. However, they have much higher elastic moduli than does natural bone. This is a critical problem, since a high elastic modulus of the materials may induce bone resorption because of their stress shielding. On the other hand, polymeric materials generally possess low elastic moduli, but none bond to living bone except for Polyactive™, which is biodegradable [6]. Therefore, new types of materials having a high bioactivity as well as mechanical strengths analogous to those of the natural bone must still be developed for load-bearing bone substitutes.

A composite (HAPEX™) of hydroxyapatite particles with high-density polyethylene (HDPE) was developed in the early 1980s as a bone substitute with analogous mechanical properties to those of the bone [7]. It is already clinically used for artificial incus bones. Some of the mechanical properties of HAPEX™, such as the tensile strength, have already been found to be desirable for its use in the body [8–10]. However, the fracture toughness and elastic modulus of HAPEX™ are lower than those of living bone. Additionally, glass – ceramic A-W-reinforced HDPE was developed in 1998 [11, 12]. The bioactivity of this composite is higher than that of HAPEX™, but its mechanical strengths are lower than that of HAPEX™.

On the other hand, hydroxyapatite-reinforced poly-(L-lactide) (PLLA) [13] has an initial bending strength of

280 MPa, which exceeds the bending strength of the human cortical bone (50 to 150 MPa), and an elastic modulus of 12 GPa, which is in the range of the elastic modulus of the human cortical bone (7 to 30 GPa) [14]. These mechanical properties of this composite, however, decrease to 200 MPa after 25 weeks in the phosphate-buffered saline because of the biodegradability of PLLA. Therefore, this composite is not useful as a load-bearing bone substitute but only for fracture-fixation devices such as pins or screws. Therefore, in order to develop a bone-repairing material with bone-like mechanical properties, it is necessary to incorporate a bioactive ceramic particulate with a high mechanical strength and elastic modulus into a nondegradable ductile matrix.

Kokubo et al. reported that titania gels with an amorphous structure did not induce apatite formation on their surfaces in a simulated body fluid (SBF), which was prepared to have an ion concentration nearly equal to that of human blood plasma (Na^+ 142.0, K^+ 5.0, Ca^{2+} 2.5, Mg^{2+} 1.5, Cl^- 147.8, HCO_3^- 4.2, HPO_4^{2-} 1.0, and SO_4^{2-} 0.5mM) [15], whereas the gels with an anatase or rutile structure induced apatite formation on their surfaces [16–18]. The deposition of apatite was more pronounced on the anatase gels than on the rutile gels. Therefore, a titania with a specific crystal structure, such as anatase, is effective in inducing apatite nucleation in a body environment.

Fillers have an important role in modifying the properties of various polymers. In polymeric materials, inorganic particles are used as fillers to improve their strength, toughness and wear properties [19]. The effect of fillers on the properties of the composites depends on their concentration and particle size and shape, as well as their interaction with the matrix. As yet, there has been no study regarding the effect of TiO_2 on the mechanical strengths of HDPE. TiO_2 has high mechanical strengths. For example, the elastic modulus of TiO_2 (300–320 GPa) is much higher than that of hydroxyapatite (86–110 GPa) [14]. So incorporating TiO_2 particles into the polymer matrix is considered to be effective to enhance the mechanical properties of the polymer matrix.

In this study, the effects of TiO_2 content on the bending, yield strengths, Young's modulus, the strain to failure, and compressive strength of TiO_2/HDPE composite were investigated. In addition, the apatite forming ability of TiO_2/HDPE composite in SBF was studied.

Materials and methods

Materials

Solvents and reagents, all of special reagent grade, were used without further purification. An anatase-type TiO_2 nanopowder was manufactured by Ishihara Sangyo Kaisha, Ltd., Mie, Japan. The phase of the TiO_2 powders was analyzed by powder X-ray diffraction. The TiO_2 particles were analyzed in terms of size using a laser scattering particle size distribution analyzer (MasterSizer 2000, MALVERN Co., Japan) and a BET–specific surface area analyzer (NOVA-2000, Yuasaionics Co., Japan). The surface chemical composition of the outermost layer of the as-received TiO_2 was analyzed by an X-ray photoelectron spectrometer (XPS) with an ESCA LAB MKII Model (VG Scientific, East Grin stead, England). An MgKα X-ray was used as the source. The photoelectron take–off angle was set at 30°. The measured binding energy was corrected by referring to that of the C1s as 285.0 eV. The zeta potential of the surface of the as-received TiO_2 was measured by laser electrophoresis with a Penmkem 501 Model in 0.01 mol/l phosphate buffer saline of pH 7.2 at 20 °C.

HDPE (Japan Polyolefins Co., Ltd., Tokyo, Japan) had the following number-average molecular weight: Mn, weight-average molecular weight in 1.2×10^4; Mw in 7.67×10^4 and z-average molecular weight; Mz in 47.6×10^4, Mw/Mn in 6.35 and Mz/Mw in 6.20. The melt flowing rate (MFR) of this polyethylene is 8.

Preparation of TiO_2/HDPE composites

The manufacturing process of the TiO_2/HDPE involved kneading and compression moulding. The filler content was set at 20, 40, 45, 50, 52, 52.5 and 55.6 vol%. These composites were denoted as TiO_2/HDPE −20, 40, 45, 50, 52, 52.5 and 55.6, respectively. HDPE was dried at 80 °C for 8 h and then kneaded at 210 °C in a batch kneader PBV 0.3 (Irie Seisaku-sho, Ltd., Tokyo, Japan). TiO_2 particles were added slowly into the melted HDPE with kneading at 210 °C in air. After adding TiO_2, the TiO_2/HDPE compound was kneaded with a 25 rpm rotation speed for 30 min.

The obtained compounds were molded at 230 °C for 1 h and then hot-pressed in air under a pressure of 2.5 MPa.

Characterization of TiO_2/HDPE composites

Mechanical test

Three-point bend testing of TiO_2/HDPE composites was performed using ten samples of each type of composite. The specimens were cut to the desired shape and then polished, using 400 grit silicon carbide paper, to a size of 40 mm × 10 mm × 4 mm. A testing machine, Model 5582 (Instron Co. Ltd., L. A., USA), was used to apply a load over a 30 mm span. Measurements were performed with a cross-head speed of 1.0 mm/min at room temperature according to JIS K 7171. The fracture surfaces were examined using a field emission scanning electron microscope (FE-SEM)

with a JSM-6330F Model (JEOL DATUM Co. Ltd., Nagoya, Japan) after coating with a thin layer of Au.

The values for bending strength, Young's modulus, yield strength and strain to failure were calculated according to the following equations: [12, 20]

$$\text{Bending strength } \sigma = 3pL/2bd^2 \quad (1)$$

$$\text{Young's modulus } E = \sigma/(6d\delta/L^2) \quad (2)$$

$$\text{Yield strength } \sigma_f = (3p_f L/2bd^2)((n+2)/3) \quad (3)$$

$$\text{Strain to failure } \varepsilon = (6d\delta/L^2)((2n+1)/n)(1/3), \quad (4)$$

where p is the load at elastic limit (N), p_f is the load at fracture (N), L is the sample length (mm), δ is the displacement of the cross head (mm), b is the sample width (mm), d is the sample height (mm) and n is a strain-hardening exponent ($0 < n < 1$).

For compressive mechanical analysis, specimens of the dimensions 10 mm × 10 mm × 4 mm were cut from the hot-pressed composite plates. They were subsequently polished using 400 grit silicon carbide papers to remove defects from the specimen surfaces. The strength measurement was carried out at a cross-head speed of 1.0 mm/min according to JIS K 7181. The tests were carried out at room temperature in air.

The compressive strength was calculated from

$$\text{Compressive strength, } \sigma_f = F/A, \quad (5)$$

where F is fracture load (N) and A is the initial cross sectional area (mm^2).

Density

The densities of the TiO_2/HDPE composites were measured by the Archimedes method using a pycnometer and a glass bottle of known volume with a capillary tube at the top as a container. The liquid medium for all materials was distilled water.

Bioactivity test

The bioactivity of the TiO_2/HDPE composites was evaluated by examining apatite formation on their surfaces in the simulated body fluid (SBF). It has been revealed that materials that form a bone-like apatite on their surfaces in SBF form the apatite even in a living body and bond to living bone through the apatite layer [21]. The bioactivity of the composite was compared with that of TiO_2 particles or pure HDPE. The TiO_2 particles were embedded on the tape stuck to a glass slide 10 mm × 10 mm × 2 mm in size. For both HDPE and TiO_2/HDPE composites, specimens of 10 mm × 10 mm × 4 mm in size were cut, polished with a 400 grit silicon carbide paper for 5 min, washed with distilled water and dried at room temperature. SBF with ion concentrations nearly equal to those of human blood plasma was prepared by dissolving the reagents NaCl, $NaHCO_3$, KCl, $K_2HPO_4 \cdot 3H_2O$, $MgCl_2 \cdot 6H_2O$, $CaCl_2$ and Na_2SO_4 (Nacalai tesque, Inc. Kyoto, Japan) in distilled water and buffered at pH7.4 and 36.5 °C with $(CH_2OH)_3CNH_2$ and 1M HCl (Nacalai tesque, Inc. Kyoto, Japan). The specimens were soaked in 30 ml of SBF at 36.5 °C. After various time periods, the specimens were removed from the fluid, washed moderately with ion-exchanged distilled water, and dried at room temperature for 1 day. Their surfaces were analyzed by thin-film X-ray diffraction (TF-XRD) with RINT Model 2000 (Rigaku Denki Co. Ltd., Tokyo, Japan). The morphology of the surface layer of the composites was observed by FE-SEM after coating them with a thin Au film.

Results

Characterization of TiO_2

The as-received TiO_2 particles were confirmed to be essentially of the anatase phase by powder X-ray diffraction analysis. They had a broad particle size distribution, with a median particle size of 535 nm. The BET surface area of the as-received TiO_2 was approximately 8.56 m^2g^{-1}. Figure 1 shows a TEM photograph of the as-received TiO_2. TiO_2 particles possessed a round shape and smooth surface. Figure 2 shows O(1s) spectra of the as-received TiO_2. Both TiO_2 and Ti-OH peaks were detected. This result indicates that the as-received TiO_2 already has Ti-OH groups, which is essential for apatite nucleation. The zeta potential of the surface of the as-received TiO_2 was found to be highly negative (−22.5 mV).

Fracture surface of composites

Figure 3 shows FE-SEM images of the fracture surfaces of TiO_2/HDPE composites with different TiO_2 contents after the bending test. As the FE-SEM image in Fig. 3a shows, at 20 vol% filler content there was a large degree of polymer deformation; this was indicated by the presence of elongated strands of polyethylene. However, with greater than 40 vol% of TiO_2 (Figs. 3b,c and d), there was a small degree of polymer deformation. Along with the formation of polymer fibrils, the particles of TiO_2 were still clearly seen within the polyethylene matrix. It was easy to detect the TiO_2 agglomerates in the TiO_2/HDPE-52 (Fig. 3c) and TiO_2/HDPE-56 (Fig. 3d).

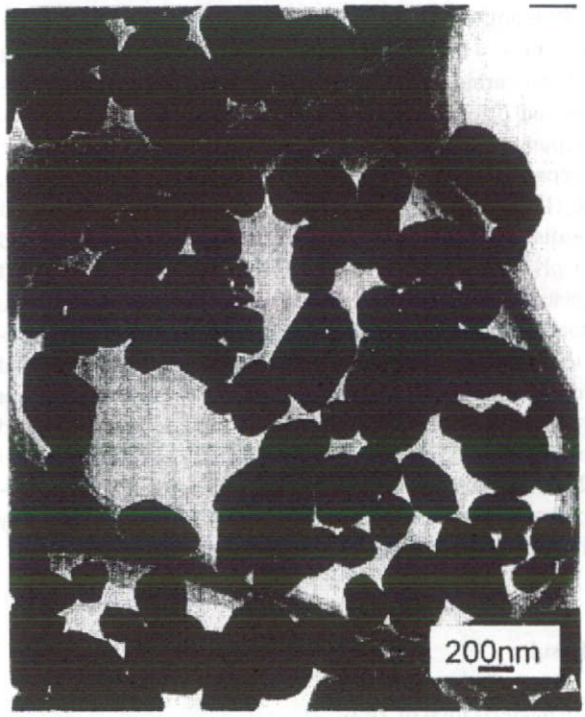

Fig. 1 Transmission electron micrograph of the as-received TiO_2 particles

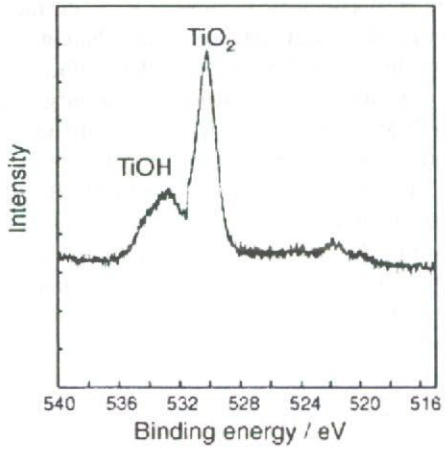

Fig. 2 O(1s) peak in the XPS spectrum of as-received TiO_2

Mechanical properties of composites

The values for bending strength, yield strength, Young's modulus, fracture strain and compressive strength of the TiO_2/HDPE composites and HDPE are shown in Table 1. The bending strength, yield strength and Young's modulus increased with increasing TiO_2 content up to 50 vol% and decreased with increasing content above 52 vol%. The yield strength and Young's modulus were, respectively, 28 MPa and 1.4 GPa for HDPE, 49 MPa and 7.6 GPa for TiO_2/HDPE-40, 54 MPa and 7.1GPa for TiO_2/HDPE-50, and 29 MPa and 6.8 GPa for TiO_2/HDPE-55.6. The strain to failure decreased as the TiO_2 content increased up to 40 vol%. However, the values obtained for the strain to failure increased for the composites with a TiO_2 content higher than 45 vol%.

The increase in the TiO_2 volume fraction resulted in an increase in compressive strength. The following compressive strengths were obtained: 22 MPa for HDPE, 61 MPa for TiO_2/HDPE-40, 75 MPa for TiO_2/HDPE-50, and 87 MPa for TiO_2/HDPE-55.6.

The representative load-displacement curves of three-point bend testing were demonstrated for TiO_2/HDPE composites in Fig. 4. Figure 4 shows that HDPE did not fracture within the limits of the three-point bending apparatus. This behavior resulted in mechanical properties, in that they had a low bending strength, yield strength and Young's modulus, and a large strain to failure. For TiO_2/HDPE-20 and TiO_2/HDPE-40, this ductile behavior was no longer a dominant feature. As the TiO_2 content increased from 40 vol%, the fracture strain also increased.

Density of composites

Figure 5 shows the densities of TiO_2/HDPE composites. Compared to the theoretical density, which was calculated by the rule of mixture, the density of TiO_2/HDPE composites with a low TiO_2 content (20 vol%) almost matched the theoretical value. However, as the amount of TiO_2 was increased up to 55.6 vol%, the discrepancy between the measured and theoretical densities increased.

Bioactivity of composites

Figure 6 shows TF-XRD patterns of TiO_2 particle (a) and HDPE (b) which were soaked in SBF for 3 and 14 days, respectively. Apatite was able to form on the TiO_2 particles after 3 days of soaking; however, it was not formed on the HDPE even after 14 days of soaking in SBF.

Figure 7 shows TF-XRD patterns of TiO_2/HDPE composites that were soaked in SBF for 14 days. Apatite peaks were detected on all of the TiO_2/HDPE composites except for those with 0 and 20 vol% of TiO_2. This result indicates that the apatite forms on TiO_2/HDPE composites with a TiO_2 content greater than 40 vol% in SBF and that apatite-forming ability increases with increasing TiO_2 content. Figure 8 shows TF-XRD patterns of a TiO_2/HDPE composite with 50 vol% of TiO_2 that was soaked in SBF for various periods up to 14 days. Small apatite peaks were detected at 7 days of soaking. With 14 days of soaking, these apatite peaks increased. This result indicates that the apatite formed on a TiO_2/HDPE composite with 50 vol% of TiO_2 increased with increasing soaking time.